PHYSICAL REVIEW A **90**, 053406 (2014)

Relativistic effects in photoionization time delay near the Cooper minimum of noble-gas atoms

Soumyajit Saha,[1] Ankur Mandal,[1] Jobin Jose,[2] Hari R. Varma,[3] P. C. Deshmukh,[1,7] A. S. Kheifets,[4] V. K. Dolmatov,[5] and S. T. Manson[6]

[1]*Department of Physics, Indian Institute of Technology Madras, Chennai 600036, India*
[2]*Department of Chemistry, Texas A & M University, College Station, Texas 77843, USA*
[3]*School of Basic Sciences, Indian Institute of Technology, Mandi 175001, India*
[4]*Research School of Physics and Engineering, The Australian National University, Canberra ACT 0200, Australia*
[5]*Department of Physics and Earth Science, University of Northern Alabama, Florence, Alabama 35632, USA*
[6]*Department of Physics and Astronomy, Georgia State University, Atlanta, Georgia 30303, USA*
[7]*Department of Physics and Astronomy, The University of Western Ontario, London, Canada N6A 3K7*

(Received 3 August 2014; published 6 November 2014)

Time delay of photoemission from valence ns, $np_{3/2}$, and $np_{1/2}$ subshells of noble-gas atoms is theoretically scrutinized within the framework of the dipole relativistic random phase approximation. The focus is on the variation of time delay in the vicinity of the Cooper minima in photoionization of the outer subshells of neon, argon, krypton, and xenon, where the corresponding dipole matrix element changes its sign while passing through a node. It is revealed that the presence of the Cooper minimum in one photoionization channel has a strong effect on time delay in other channels. This is shown to be due to interchannel coupling.

DOI: 10.1103/PhysRevA.90.053406 PACS number(s): 32.80.Rm, 32.80.Fb, 42.50.Hz

I. INTRODUCTION

Time delay in atomic photoionization refers to a slight temporal delay in the release of the photoelectron wave packet upon absorption of a short electromagnetic pulse. This delay is very small, of the order of attoseconds (as). This opens a unique road towards calibration of various measuring devices that can capture electron motion in atoms, molecules, and solids on the attosecond time scale that would be difficult to do otherwise. These devices are known as the attosecond streak camera [1,2], the angular streaking attoclock [3], and the RABITT (reconstruction of attosecond bursts by ionization of two-photon transitions) [4]. In these devices, the phase-stabilized electric field of a short laser pulse is used to convert the release time of the outgoing electron wave packet into other measurable quantities such as kinetic energy (attosecond streak camera), the momentum vector (angular streaking attoclock), or the beating signal of the electron detector (RABITT).

To date, the relative time delay of photoemission from neighboring valence atomic sub-shells has been measured with a high accuracy in neon [5] and argon [4,6]. The relative time delay between the outer shells of the atomic pairs (He vs Ne and Ne vs Ar) can now be determined owing to active stabilization of the RABITT spectrometer [7]. Similar measurements can be performed in heavier noble-gas atoms relative to the time delay in the $1s$ subshell of He [8]. The high-order-harmonics-generation (HHG) technique has also been used to determine the time delay in Ar [9].

The concept of time delay was introduced in the early works of Eisenbud [10] and Wigner [11] in the context of the phase-shift analysis of slow electron s-wave scattering. The focus of the Eisenbud-Wigner theory was the group velocity of a wave packet [12]. Typically, a free-electron wave packet, which is made up of the superposition of plane waves with different energies $E = k^2/2$ emerging at a point x_0, spreads with time, even in vacuum. (Note the use of atomic units in which $e = m = \hbar = 1$ throughout the paper.) Its peak propagates at the group velocity $v_g = d\omega/dk|_{k=k_0}$. Here, k_0 is the mean momentum of the free electron that contributes to the wave packet. When the free-electron wave packet elastically scatters off a potential, a peak of the transmitted wave packet propagates at the *same* group velocity $v_g = d\omega/dk|_{k=k_0}$ as before scattering. The corresponding transmission amplitude T is generally complex, $T = |T|e^{i\varphi_T}$, with φ_T being the amplitude's phase. Due to the phase factor in T, the transmitted wave packet appears to have originated at a *different* point, namely, at $x_0 - d\varphi_T/dk|_{k_0}$, rather than at x_0. The term $d\varphi_T/dk|_{k_0}$ in the above expression determines the *spatial* phase shift $x_{\rm shift} = d\varphi_T/dk|_{k_0}$. It provides a measure for the time delay $t_{\rm delay}$ due to electron scattering:

$$t_{\rm delay} = \frac{x_{\rm shift}}{v_g} = \frac{d\varphi_T/dk|_{k_0}}{d\omega/dk|_{k=k_0}} = \frac{d\varphi_T}{dE}\Big|_{E_0}, \qquad (1)$$

where E_0 is the mean energy of the wave packet. As shown earlier [13], time delay in a collision process, defined in terms of an energy derivative of the phase shift, is the same as collision lifetime. Therefore the former serves as a temporal measure of the complex system which emerges due to photoabsorption and the subsequent decay by emitting a photoelectron from the atomic complex. In recent years, accurate numerical calculation of atomic time delay has become an *ad hoc* topic of intense theoretical studies [14–18].

II. METHODOLOGY

In the present paper, atomic photoionization is calculated using *incoming boundary conditions* for the final continuum state wave functions. These ion-plus-photoelectron final states are related to the wave function for elastic electron-ion scattering through time-reversal symmetry [19]. In the relativistic random-phase approximation (RRPA), an electron transition due to photoionization is described by a dipole matrix element which is generally complex [20,21]. In particular, for a transition from an initial bound state $|n,\kappa\rangle$ to a continuum

TABLE I. Dirac-Hartree-Fock (DHF) and experimental [22] subshell thresholds.

Atom	Subshell	DHF a.u.	Expt. a.u.
Ne	$2p_{\frac{3}{2}}$	0.848	0.794
	$2p_{\frac{1}{2}}$	0.853	0.797
	$2s$	1.936	1.948
Ar	$3p_{\frac{3}{2}}$	0.588	0.579
	$3p_{\frac{1}{2}}$	0.595	0.586
	$3s$	1.287	1.077
	$2p_{\frac{3}{2}}$	9.547	
	$2p_{\frac{1}{2}}$	9.631	
	$2s$	12.411	
Kr	$4p_{\frac{3}{2}}$	0.514	0.514
	$4p_{\frac{1}{2}}$	0.542	0.540
	$4s$	1.188	1.010
	$3d_{\frac{5}{2}}$	3.727	
	$3d_{\frac{3}{2}}$	3.777	
Xe	$5p_{\frac{3}{2}}$	0.439	0.444
	$5p_{\frac{1}{2}}$	0.493	0.492
	$5s$	1.0101	0.859
	$4d_{\frac{5}{2}}$	2.634	
	$4d_{\frac{3}{2}}$	2.711	

state $|E,\overline{\kappa}\rangle$, the dipole matrix element is given by

$$\langle E,\overline{\kappa}|\,\hat{d}\,|n\kappa\rangle = i^{1-\overline{\ell}}e^{i\delta_{\overline{\kappa}}}\langle E,\overline{\kappa}\|\,Q_1^{(1)}\|n\kappa\rangle\,. \tag{2}$$

Here, $\langle E,\overline{\kappa}\|\,Q_1^{(1)}\|n\kappa\rangle$ is the reduced matrix element and $\delta_{\overline{\kappa}}$ is the phase shift of the final-state continuum wave function with incoming boundary conditions. Since the photoionization matrix element is generally complex, the energy-dependent phase shifts $\delta_{\overline{\ell}}(E)$ of a partial ℓ-electronic wave is defined by

$$\delta_{\overline{\ell}}(E) = \tan^{-1}\left\{\frac{\mathrm{Im}\langle E,\overline{\kappa}|\,\hat{d}\,|n\kappa\rangle}{\mathrm{Re}\langle E,\overline{\kappa}|\,\hat{d}\,|n\kappa\rangle}\right\}. \tag{3}$$

The quantity $d\delta_{\overline{\ell}}(E)/dE$ then provides a measure of time delay occurring in various dipole photoionization channels.

Ab initio RRPA [20,21] accounts, reliably, both for relativistic effects, such as the initial and final state spin-orbit splitting and major many-body correlations. The latter are particularly important to the calculations of this paper, since phase shifts $\delta_{\overline{\ell}}(E)$ are known to be quite sensitive to correlation in the form of interchannel coupling. Therefore a reliable accounting for this aspect of correlation is vital for an adequate study of the time delay phenomenon.

In the present RRPA calculations of photoionization matrix elements and photoelectron phase shifts, experimental ionization thresholds were substituted into the RRPA equations. Corresponding ionization thresholds for Ne, Ar, Kr, and Xe are presented in Table I. Furthermore, the following number of relativistic dipole photoionization channels were accounted for in corresponding RRPA calculations of photoionization of these atoms: (a) for Ne, seven channels which originate due to photoionization of the $2p$ and $2s$ subshells; (b) for Ar, 14 channels (from $3p$, $3s$, $2p$ and $2s$ sub-shells); whereas (c) both for Kr and Xe, 13 channels (from the $4p$, $4s$, $3d$ subshells of Kr and $5p$, $5s$, $4d$ subshells of Xe) were coupled in the *truncated* RRPA. Note that the omitted channels, being far away energetically, should be unimportant in the energy ranges considered; this is substantiated by the excellent agreement between the length and velocity forms of the dipole matrix elements.

III. RESULTS AND DISCUSSION

A. Photoionization cross sections, phase shifts, and time delays

In this section, RRPA calculated results for the photoionization cross sections, phase shifts, and time delays in valence shells of Ne, Ar, Kr, and Xe are presented. Moreover, in order to understand the importance of relativistic effects, these results are compared with corresponding calculated results of work [17] which was obtained, as in [23], within the framework of a nonrelativistic random phase approximation (RPAE) [24]. In this way, the role of relativistic effects will be elucidated in a consistent manner in view of the complete equivalency between RPAE and RRPA in accounting both for direct and exchange interactions; the only difference in the two methodologies is the inclusion of relativistic effects in the RRPA. In RPAE, the expression for the photoionization amplitude is given by

$$f_{n_il_i}(E) \propto \sum_{\substack{l=l_i\pm1\\ m=m_i}} e^{i\delta_l} i^{-l} Y_{lm}(\hat{k})\,(-1)^m \begin{pmatrix} l & 1 & l_i \\ -m & 0 & m_i \end{pmatrix} \times \langle El\|\,D\|n_il_i\rangle. \tag{4}$$

Here, the reduced dipole matrix element, which is stripped of all the angular momentum projections, is defined as

$$\langle El\|\,r\,\|n_il_i\rangle = \hat{l}\hat{l}_i \begin{pmatrix} l & 1 & l_i \\ 0 & 0 & 0 \end{pmatrix} \int r^2 dr\, R_{El}(r)\, r\, R_{n_il_i}(r)\,, \tag{5}$$

where $\hat{l} \equiv \sqrt{2l+1}$. In the present work, the amplitude $f(E)$ is evaluated in the forward direction $k\|\hat{z}$, which is usually the case in the attosecond time delay measurements. In the relativistic case, we use the same expression (4) in which the orbital momenta of the initial bound state and the final continuum state are substituted by their relativistic counterparts $\ell \to j = \ell + 1/2$.

The photoelectron group delay, which is the energy derivative of the phase of the complex photoionization amplitude, gives an alternative access to the phase information. It is evaluated as

$$\tau = \frac{d}{dE}\arg f(E) \equiv \mathrm{Im}[f'(E)/f(E)]\,. \tag{6}$$

Note that when a single channel dominates, the time delay (1) reduces to the energy derivative of the phase of that channel. However, in the general case, when more than one amplitude contributes materially to the cross section from a given initial state, the phase in question is the phase of the photoionization amplitude (4). The derivative of that phase is the essence of the time delay. In other words, the phase is essentially a weighted average of the phases of the respective channels. Thus the time delay is a weighted average of the individual channel time delays. Furthermore, in such a case, Eq. (4) shows that the time delay is angular dependent.

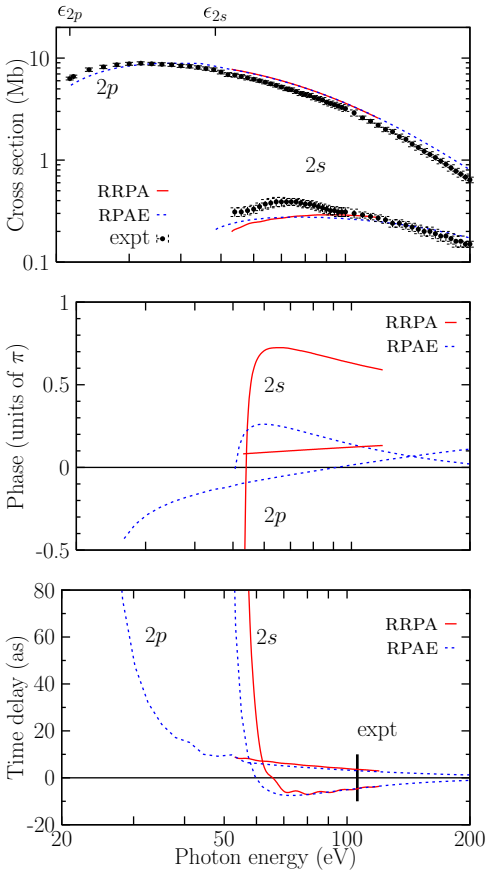

FIG. 1. (Color online) (Top) the partial photoionization cross sections of the $2s$ and $2p$ subshells of Ne. The RRPA and RPAE calculations are shown by the solid (red) and dashed (blue) lines, respectively. The recommended experimental data by Bizau and Wuilleumier [25] are displayed by filled circles with error bars. (Middle) Phases in the photoionization amplitudes arg $f_{2s}(E)$ and arg $f_{2p}(E)$ evaluated in the $\hat{z}$ direction. The same line styles are used for the RPAE and RRPA calculations. (Bottom) The phase derivatives are converted into the units of the group delay. The length of the vertical bar at the photon energy of 106 eV visualizes the relative time delay between the $2p$ and $2s$ subshells of 21 ± 5, as measured by Schultze *et al.* [5].

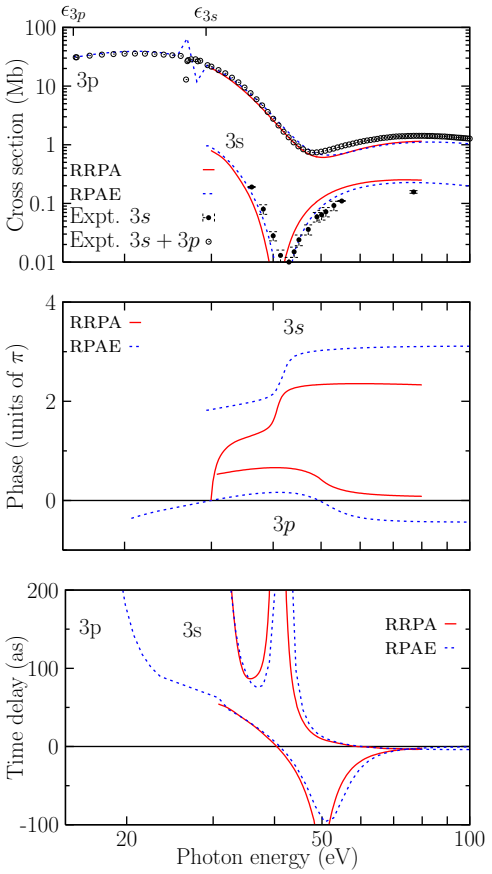

FIG. 2. (Color online) (Top) The partial photoionization cross sections of the $3s$ and $3p$ subshells of Ar. The RPAE and RRPA calculations are shown by the dashed (blue) and solid (red) lines, respectively. The experimental data for $3s$ [26] and for $3s + 3p$ [27] are displayed by filled circles with error bars and open circles, respectively. (Middle) Phases in the photoionization amplitudes arg $f_{3s}(E)$ and arg $f_{3p}(E)$ evaluated in the $\hat{z}$ direction. The same line styles are used for the RPAE and RRPA calculations. (Bottom) The phase derivatives are converted into the units of the group delay.

1. Neon

On the top panel of Fig. 1 we present the partial photoionization cross sections of valence-shell photoionization of Ne. The RRPA cross sections are shown by the solid (red) lines and the RPAE cross sections are exhibited by the dashed (blue) line. The recommended experimental data by Bizau and Wuilleumier [25] are displayed by filled circles with error bars. On the middle panel, we use the same line style to show the phases of the photoionization amplitudes $f_{2s}(E)$ and $f_{2p}(E)$ evaluated in the $\hat{z}$ direction. The bottom panel of Fig. 1 displays the photoelectron group delay calculated as the energy derivative of the phase of the corresponding photoionization amplitude evaluated in the z-axis direction. Photoemission from the $2s$ subshell seems to be ahead of that of the $2p$ subshell at around the 100-eV photon energy mark where the measurement of Schultze *et al.* [5] was taken (shown as a vertical bar in the figure).

2. Argon

An analogous set of data for Ar $3s$ and $3p$ subshells is shown in Fig. 2. On the top panel we make a comparison of the RRPA (solid red line) and RPAE (dashed blue line) partial photoionization cross sections with the experimental data of Möbus *et al.* [26] for the $3s$ subshell and by Samson and Stolte [27] for the sum of $3s$ and $3p$ subshells. These partial photoionization cross sections are qualitatively different from those of Ne shown in Fig. 1. First, the $3p$ cross section in Ar displays the Cooper minimum whereas the nodeless $2p$ orbital does not [28]. Second, the inner-shell correlation completely changes the $3s$ cross section in magnitude and shape and introduces a deep Cooper-like minimum at a slightly smaller photon energy. Both the RRPA and RPAE calculations reproduce these features in fair agreement with the experiment. We note that the total cross-section measurement of Samson and Stolte [27] includes ionization leading to the ionic ground state as well as ionization with excitation. The former process, not included in the present calculations, seems to be insignificant, as can be seen by a good agreement between

the both theories and the experiment. This also means that the total cross section is dominated by the $3p$ shell in this energy region.

The RRPA and RPAE phases in Ar, shown in the middle panel of Fig. 2 are very different from Ne. When the cross section goes through the Cooper minimum, the corresponding phase makes a jump of about π in the $3s \rightarrow \varepsilon p$ amplitude and $-\pi$ in the $3p \rightarrow \varepsilon d$ amplitude. This jump is easy to understand. If the amplitude was real and had a node, it would simply change its sign, which would amount to adding a phase factor of π in the complex number representation.

This jump of π has a dramatic effect on the time delay, which is shown on the bottom panel of Fig. 2. It drives the time delay in the $3s$ subshell to much larger numbers, of the order of several hundreds of attoseconds. The situation is less dramatic for the $3p$ subshell. Here the normally weak transition $3p \rightarrow \varepsilon s$ takes over near the Cooper minimum of the strong $3p \rightarrow \varepsilon d$ transition, and the resulting time delay does not go below –100 as, as in the RPAE calculation. This minimum is somewhat deeper in the RRPA calculation.

Note that the Cooper minimum in the $3s$ photoionization channel in the 50-eV region arises solely due to interchannel coupling with the $3p$ photoionization channels [29]. Thus, the change of phase by $\sim\pi$ in the $3s$ channel and the resultant huge time delay are part and parcel of the "transfer" of the Cooper minimum from the $3p$ to the $3s$ channels via correlation in the form of interchannel coupling.

3. Krypton

On the top panel of Fig. 3, we display the partial photoionization cross sections of the $4s$, $4p$, and $3d$ subshells of Kr calculated in the RRPA and RPAE models [shown by the solid (red) and dotted (blue) lines, respectively]. Note that the energy regions around 27.48 eV ($4s_{1/2}$ threshold) and from 101.41 eV ($3d_{5/2}$ threshold) to 102.80 eV ($3d_{3/2}$ threshold) are skipped because they fall into the region of autoionization resonances. Comparison is made with the experimental data by Ehresmann *et al.* [30] for $4s$ (displayed by filled circles with error bars), by Samson and Stolte [27] for the total $4s + 4p + 3d$ cross section (shown by open circles), and by Aksela *et al.* [31] for $3d$ (displayed with asterisks). Good agreement between the two calculations can be seen for the $4p$ and $3d$ subshells which dominate the total cross section in their respective energy ranges. The Cooper minimum of the $4s$ subshell is slightly displaced between the two calculations.

On the middle panel of Fig. 3 we display the phases of the photoionization amplitudes calculated in the same two models. Here agreement is not so close as for the cross section. This demonstrates a greater sensitivity of the phase of the matrix elements to the details of the calculation in comparison with their squared moduli (cross sections).

On the bottom panel of Fig. 3 the phase shifts are converted into photoemission time delays according to Eq. (1). The time delays are qualitatively similar in the two models. However, some important differences can be clearly seen. More specifically, the sharp peak in the $4s$ time delay near the Cooper minimum of the partial photoionization cross section is shifted between the two calculations.

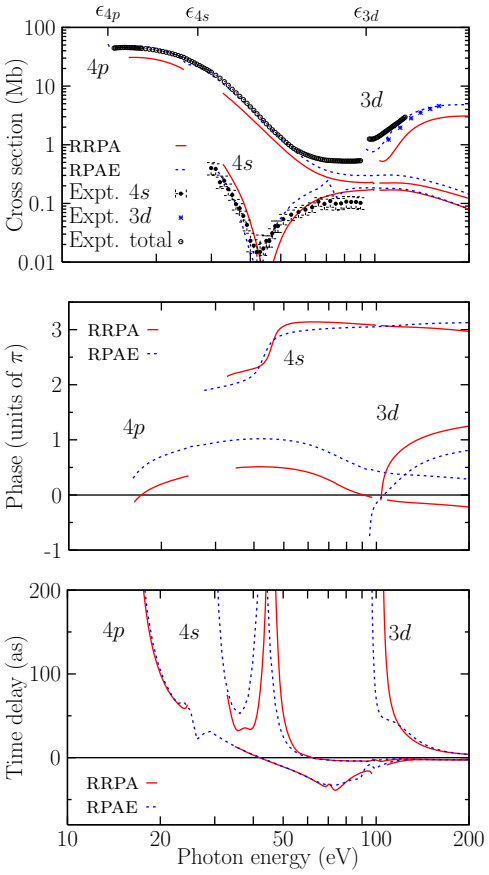

FIG. 3. (Color online) (Top) The partial photoionization cross sections of Kr. The RRPA and RPAE calculations are shown by the solid (red) and dashed (blue) lines, respectively. The experimental data by Ehresmann *et al.* [30] for $4s$ are displayed by filled circles with error bars and the total cross-section data by Samson and Stolte [27] are shown with open circles. The data from Aksela *et al.* [31] for $3d$ are displayed with asterisks. (Middle) Phases in the photoionization amplitudes evaluated in the $\hat{z}$ direction. The same line styles are used for the RPAE and RRPA calculations. (Bottom) The phase derivatives are converted into the units of the time delay.

4. Xenon

On the top panel of Fig. 4 we display the partial photoionization cross sections of the $5s$, $5p$, and $4d$ subshells of Xe calculated in the RRPA (red solid lines) and RPAE (blue dashed lines) models. Note that the energy regions around 23.37 eV ($5s_{1/2}$ threshold) and from 71.66 eV ($4d_{5/2}$ threshold) to 73.77 eV ($4d_{3/2}$ threshold) are skipped because because they fall into the region of autoionization resonances. Comparison is made with the experimental data from Becker *et al.* [32] and Fahlman *et al.* [33] for the $5s$ and $5p$ shells, and the experimental data from Becker *et al.* [32] and Lindle *et al.* [34] for the $4d$ shell. Good agreement between the two calculations can be seen for the $5p$ and $4d$ subshells. However, the Cooper minimum of the $5s$ shell is displaced between the two calculations.

On the middle panel of Fig. 4 we display the partial photoionization phase shifts in the $5s$, $5p$, and $4d$ subshells of Xe calculated in the same two models. Here agreement is not so straightforward as for the cross section.

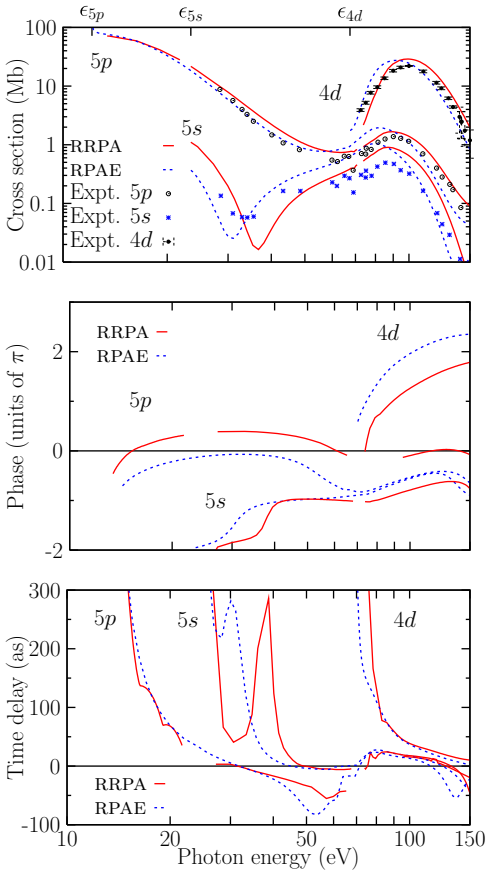

FIG. 4. (Color online) (Top) The partial photoionization cross sections of Xe. The RRPA and RPAE calculations are shown by the solid (red) and dashed (blue) lines, respectively. The experimental data for the $5p$ shell by Becker *et al.* [32] and Fahlman *et al.* [33] are shown with open circles. The experimental data of the same authors for the $5s$ shell are shown with asterisks. The experimental data by Becker *et al.* [32] and Lindle *et al.* [34] for the $4d$ shell are shown by filled circles with error bars. (Middle) The partial photoionization phase shifts for the $5s$, $5p$, and $4d$ channels. (Bottom) The phase derivatives are converted into the units of the time delay.

On the bottom panel of Fig. 4 the phase shifts are converted into photoemission time delays according to Eq. (1). The time delays are qualitatively similar in the two models. However, some important differences can be clearly seen. More specifically, the Cooper minimum shift of the $5s$ subshell is seen very clearly.

B. Intershell time delay difference

In this section, we present the results of our calculations of time delay difference between the $2s$ and $2p$ shells in Ne and $3s$ and $3p$ shells in Ar.

1. Neon

The time delay difference between the $2s$ and $2p$ subshells of Ne is shown in Fig. 5. This difference is fairly large near the $2s$ threshold, indicative of the fact that the low-energy $2s$ photoelectron takes a longer time to exit compared to the higher energy $2p$ electron. As the photon energy increases, it is

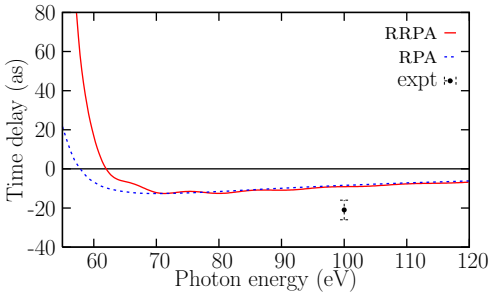

FIG. 5. (Color online) The time delay difference between the $2s$ and $2p$ subshells of neon in the RRPA and RPAE calculations. The experimental data point (filled square with error bar) is from [5].

the photoelectron time delay in the $2p$ shell, which is smaller than that of the $2s$ subshell.

The *measured value* of the time delay between photoionization channels from the $2s$ and $2p$ subshells of neon at the photon energy of 100 eV is 21 ± 10 as [5]. The RRPA prediction is about 10 as, which is only half of the experimental value. It is smaller in comparison to the large time delay difference in the near-threshold region. It seems that the contribution to the experimentally measured time delay comes from two processes: (i) the delay *difference* in the single photon ionization channel and (ii) the time delay associated with the two-photon ionization channel, sometimes referred to as the continuum-continuum (CC) [6] or Coulomb-laser coupling (CLC) [35] corrections. The RRPA accounts for the part of the time delay associated with the single-photon process. However, the CC, or equivalently, CLC, correction accounts for only 3.5 as in Ref. [35] and cannot reconcile the difference between the measured and calculated time delay difference between the $2s$ and $2p$ shells. Similar conclusions were reached in previous numerical studies [15–18].

2. Argon

The time delay difference between the $3s$ and $3p$ subshells of Ar is given in Fig. 6. Near the $3s$ threshold, the $3s$ electrons escape somewhat more slowly compared to the $3p$ electrons. The rapid change in the scattering phase shift near the Cooper minimum affects the time delay between the $3s$ and $3p$ electrons.

The time delay predicted by the RRPA is compared with those measured by Klünder *et al.* [4]. From the experimental

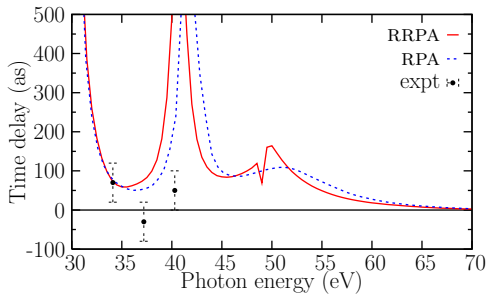

FIG. 6. (Color online) The time delay difference between the $3s$ and $3p$ subshells of argon. The nonrelativistic RPAE calculation (blue solid line) is from [17]. The experimental data (filled circles with error bars) are from [6].

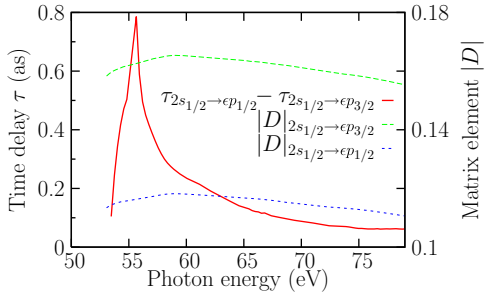

FIG. 7. (Color online) The time delay difference between the two relativistic channels $2s_{1/2} \to \epsilon p_{1/2}$ and $2s_{1/2} \to \epsilon p_{3/2}$ in neon (red solid line, left y axis). The moduli of the corresponding transition matrix elements are plotted with the blue dotted and green dashed lines, respectively (right y axis).

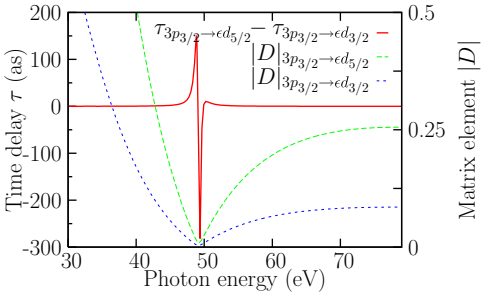

FIG. 8. (Color online) The time delay difference between the two relativistically split channels $3p_{3/2} \to \epsilon d_{3/2}$ and $3p_{3/2} \to \epsilon d_{5/2}$ in Ar (red solid line, left y axis). The moduli of the corresponding transition matrix elements are plotted with the blue dotted and green dashed lines, respectively (right y axis).

results, time delay for the single-photon ionization channel is extracted and plotted. There is fairly good agreement between the RRPA result and experimental observations. Near the Cooper minimum, the experimental result shows an enhancement in time delay, in response to the presence of Cooper minimum. Unfortunately, there is a scarcity of experimental data to verify the behavior of time delay near the Cooper minimum region.

C. Interchannel time delay difference

In this section, we show our results for the time delay difference between the two relativistically split channels. This difference is particularly strong near the Cooper minima in the respective photoionization cross sections.

1. Neon

The neon $2s$ photoionization cross section, shown in Fig. 7, does not have a Cooper minimum which is displaced to the discrete part of the spectrum. Hence the cross section increases gradually from the threshold. Nevertheless, the hidden Cooper minimum causes a noticeable time-delay difference between the two relativistic channels $2s_{1/2} \to \epsilon p_{1/2}$ and $2s_{1/2} \to \epsilon p_{3/2}$. Calculations were done at a number of energy points, and the sharp structure therefore may not be just numerical noise. It might be due to a slight difference in the positions of the Cooper minima, even though they are in the discrete spectrum.

2. Argon, krypton, and xenon

In Fig. 8 we show the time delay difference between the two relativistically split channels $3p_{3/2} \to \epsilon d_{3/2}$ and $3p_{3/2} \to \epsilon d_{5/2}$. Near the $3p_{3/2} \to \epsilon d_{3/2}$ Cooper minimum, this time delay difference is positive, whereas it is negative near the $3p_{3/2} \to d_{5/2}$ Cooper minimum. The Cooper minima positions are indicated by the moduli plot of the corresponding transition matrix elements. The strong variation of the time delay difference indicates the importance of employing a relativistic formalism.

The time delay of photoemission relative to absorption of the photon in the $3p_{3/2} \to \epsilon d_{5/2}$ channel occurs somewhat (a few hundreds of attoseconds) later than in the $3p_{3/2} \to \epsilon d_{3/2}$ channel into the region of the $3p_{3/2} \to \epsilon d_{3/2}$ Cooper minimum. Here, $3p_{3/2} \to \epsilon d_{3/2}$ is the quicker exit channel with less time delay. Likewise, photoionization in the $3p_{3/2} \to \epsilon d_{3/2}$ channel occurs somewhat later than in the $3p_{3/2} \to \epsilon d_{5/2}$ channel into the region of $3p_{3/2} \to \epsilon d_{5/2}$ Cooper minimum. Here, $3p_{3/2} \to \epsilon d_{3/2}$ is the slower exit channel.

Very similar tendencies in the interchannel time delay difference near the respective Cooper minima can be seen in Fig. 9 for Kr and in Fig. 10 for Xe. Owing to increasing spin-orbit splitting, the difference in the Cooper minima positions is larger in these heavier atoms and, therefore, the interchannel time delay difference is more prominent.

IV. CONCLUSIONS

In the present work, the photoelectron group time delay in valence-shell photoionization of the noble-gas atoms of Ne, Ar, Kr, and Xe were theoretically studied within the framework of the fully relativistic RRPA methodology. Moreover, for a better understanding of the importance of relativistic effects, a comparison was performed between corresponding nonrelativistic RPAE calculations [17]. In addition, to control the accuracy of the present results, comparison was made with available experimental data for the partial photoionization cross sections and intershell time delays. It was demonstrated that relativistic effects manifest themselves particularly strongly near a Cooper minimum, where a large difference in time delay was revealed between spin-orbit split exit channels. Specifically, it was found that near a Cooper minimum in the $np_{3/2} \to \epsilon d_{3/2}$ channel, a photoelectron leaves the atom sooner via the

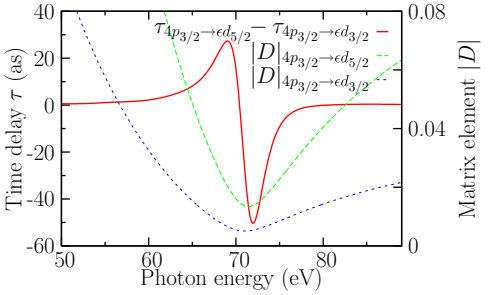

FIG. 9. (Color online) Same as in Fig. 8 for the relativistically split channels $4p_{3/2} \to \epsilon d_{3/2}$ and $4p_{3/2} \to \epsilon d_{5/2}$ in Kr.

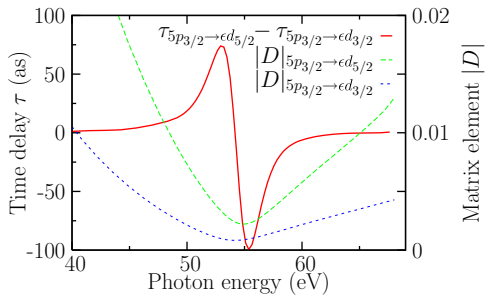

FIG. 10. (Color online) Same as in Fig. 8 for the relativistically split channels $5p_{3/2} \to \epsilon d_{3/2}$ and $5p_{3/2} \to \epsilon d_{5/2}$ in Xe.

$np_{3/2} \to \epsilon d_{3/2}$ channel than via the $np_{3/2} \to \epsilon d_{5/2}$ channel and vice versa. Furthermore, it was discovered that the time-delay difference between two relativistically split exit channels is largest for Ar (about two hundred as), smallest in Kr (about 30 as), and intermediate (about 50 as) for Xe. Further studies are necessary to determine if there is any systematic trend in the time-delay phenomenon along a sequence of atoms with progressively increasing atomic numbers. Inclusion of the nondipole terms to the interaction Hamiltonian, as in Ref. [36], is also desirable for the completeness of the study.

ACKNOWLEDGMENTS

This work was supported by the Department of Science and Technology (DST), Government of India, by the National Science Foundation, by the Department of Energy, Office of Chemical Sciences, and by the Australian Research Council. One of the authors (J.J.) is thankful to IIT-Mandi for the hospitality and support he received for a part of this work that was done at Mandi.

[1] A. Baltuška *et al.*, Nature (London) **421**, 611 (2003).
[2] R. Kienberger *et al.*, Nature (London) **427**, 817 (2004).
[3] P. Eckle *et al.*, Nat. Phys. **4**, 565 (2008).
[4] K. Klünder, J. M. Dahlström, M. Gisselbrecht, T. Fordell, M. Swoboda, D. Guénot, P. Johnsson, J. Caillat, J. Mauritsson, A. Maquet, R. Taïeb, and A. L'Huillier, Phys. Rev. Lett. **106**, 143002 (2011).
[5] M. Schultze, M. Fiess, N. Karpowicz, J. Gagnon, M. Korbman, M. Hofstetter, S. Neppl, A. L. Cavalieri, Y. Komninos, Th. Mercouris, C. A. Nicolaides, R. Pazourek, S. Nagele, J. Feist, J. Burgdörfer, A. M. Azzeer, R. Ernstorfer, R. Kienberger, U. Kleineberg, E. Goulielmakis, F. Krausz, and V. S. Yakovlev, Science **328**, 1658 (2010).
[6] D. Guénot, K. Klünder, C. L. Arnold, D. Kroon, J. M. Dahlström, M. Miranda, T. Fordell, M. Gisselbrecht, P. Johnsson, J. Mauritsson *et al.*, Phys. Rev. A **85**, 053424 (2012).
[7] D. Guénot, D. Kroon, M. Kotur, E. Balogh, E. W. Larsen, J. M. Dahlstrom, J. Mauritsson, M. Gisselbrecht, E. Lindroth, and K. Varju, J. Phys. B (to be published).
[8] C. Palatchi, J. M. Dahlström, A. S. Kheifets, P. Agostini, and L. F. DiMauro, J. Phys. B (to be published).
[9] S. B. Schoun, R. Chirla, J. Wheeler, C. Roedig, P. Agostini, L. F. DiMauro, K. J. Schafer, and M. B. Gaarde, Phys. Rev. Lett. **112**, 153001 (2014).
[10] L. Eisenbud, Ph.D. thesis, Princeton University, 1948.
[11] E. P. Wigner, Phys. Rev. **98**, 145 (1955).
[12] H. Friedrich, *Theoretical Atomic Physics* (Springer-Verlag, Berlin, 2006).
[13] F. T. Smith, Phys. Rev. **118**, 349 (1960).
[14] A. S. Kheifets and I. A. Ivanov, Phys. Rev. Lett. **105**, 233002 (2010).
[15] L. R. Moore, M. A. Lysaght, J. S. Parker, H. W. van der Hart, and K. T. Taylor, Phys. Rev. A **84**, 061404 (2011).
[16] J. M. Dahlström, T. Carette, and E. Lindroth, Phys. Rev. A **86**, 061402 (2012).
[17] A. S. Kheifets, Phys. Rev. A **87**, 063404 (2013).
[18] J. Feist, O. Zatsarinny, S. Nagele, R. Pazourek, J. Burgdörfer, X. Guan, K. Bartschat, and B. I. Schneider, Phys. Rev. A **89**, 033417 (2014).
[19] P. C. Deshmukh, D. Angom, and A. Banik, *Atomic and Molecular Physics DST-SERC School* (Narosa Publication House, New Delhi, 2012).
[20] W. R. Johnson and C. D. Lin, Phys. Rev. A **20**, 964 (1979).
[21] A. Derevianko, W. Johnson, and K. Cheng, Atomic Data and Nuclear Data Tables, **73**, 153 (1999).
[22] Y. Ralchenko, A. E. Kramida, J. Reader, and NIST ASD Team, NIST Atomic Spectra Database (version 3.1.5), Technical Report, National Institute of Standards and Technology, Gaithersburg, MD (2011), URL http://physics.nist.gov/asd.
[23] M. Y. Amusia and N. A. Cherepkov, *Many-Electron Correlations in the Scattering Processes*, Case Studies in Atomic Physics Vol. 5 (North-Holland, Amsterdam, 1975), pp. 47–179.
[24] M. Y. Amusia and L. V. Chernysheva, *Computation of Atomic Processes: A Handbook for the ATOM Programs* (Institute of Physics Publishing, Bristol, UK, 1997).
[25] J. Bizau and F. Wuilleumier, J. Electron Spectrosc. Relat. Phenom. **71**, 205 (1995).
[26] B. Möbus, B. Magel, K.-H. Schartner, B. Langer, U. Becker, M. Wildberger, and H. Schmoranzer, Phys. Rev. A **47**, 3888 (1993).
[27] J. Samson and W. Stolte, J. Electron Spectrosc. Relat. Phenom. **123**, 265 (2002).
[28] U. Fano and J. W. Cooper, Rev. Mod. Phys. **40**, 441 (1968).
[29] M. Y. Amusia, V. K. Ivanov, N. A. Cherepkov, and L. V. Chernysheva, Phys. Lett. A **40**, 361 (1972).
[30] A. Ehresmann, F. Vollweiler, H. Schmoranzer, V. L. Sukhorukov, B. M. Lagutin, I. D. Petrov, G. Mentzel, and K. H. Schartner, J. Phys. B **27**, 1489 (1994).
[31] S. Aksela, H. Aksela, M. Levasalmi, K. H. Tan, and G. M. Bancroft, Phys. Rev. A **36**, 3449 (1987).
[32] U. Becker, D. Szostak, H. G. Kerkhoff, M. Kupsch, B. Langer, R. Wehlitz, A. Yagishita, and T. Hayaishi, Phys. Rev. A **39**, 3902 (1989).
[33] A. Fahlman, M. O. Krause, T. A. Carlson, and A. Svensson, Phys. Rev. A **30**, 812 (1984).
[34] D. W. Lindle, T. A. Ferrett, P. A. Heimann, and D. A. Shirley, Phys. Rev. A **37**, 3808 (1988).
[35] S. Nagele, R. Pazourek, J. Feist, K. Doblhoff-Dier, C. Lemell, K. Tökési, and J. Burgdörfer, J. Phys. B **44**, 081001 (2011).
[36] I. A. Ivanov and A. S. Kheifets, Phys. Rev. A **89**, 043405 (2014).